

# A modern halo streaming model for redshift space distortions

Cheng-Zong Ruan<sup>1,2\*</sup>, Baojiu Li<sup>1†</sup>, Carlton M. Baugh<sup>1,3</sup>, Sownak Bose<sup>1</sup>,  
Alexander Eggemeier<sup>4</sup> and David F. Mota<sup>2</sup>

<sup>1</sup>*Institute for Computational Cosmology, Department of Physics, Durham University, South Road, Durham DH1 3LE, UK*

<sup>2</sup>*Institute of Theoretical Astrophysics, University of Oslo, 0315 Oslo, Norway*

<sup>3</sup>*Institute for Data Science, Durham University, South Road, Durham DH1 3LE, UK*

<sup>4</sup>*Universität Bonn, Argelander-Institut für Astronomie, Auf dem Hügel 71, 53121 Bonn, Germany*

Accepted XXX. Received YYY; in original form 12th March 2026

## ABSTRACT

Accurate modelling of redshift-space distortions (RSD) in galaxy clustering is essential for extracting cosmological information from current and forthcoming large-scale structure surveys. While perturbation theory is reliable on large scales, much of the constraining power lies at intermediate and small separations, where nonlinear dynamics within and between dark matter haloes dominate. We present a halo streaming model for nonlinear galaxy clustering in redshift space that is accurate and physically interpretable. Our framework combines the streaming model for RSD with a halo-model decomposition of the galaxy clustering into central/satellite and one-/two-halo contributions. We build dedicated emulators for the key physical ingredients, trained on a suite of  $N$ -body simulations: halo mass functions, real-space halo two-point correlation functions, and pairwise velocity moments. By emulating these modular building blocks rather than the final redshift-space observable, this approach preserves physical transparency, enables targeted optimisation for each ingredient, and remains flexible to changes in tracer populations and galaxy-halo connection models. The resulting halo streaming model reproduces the simulated nonlinear anisotropic clustering signal down to highly nonlinear scales, while achieving the computational efficiency required for cosmological parameter inference. This framework is designed to support full-shape RSD analyses for surveys such as DESI and *Euclid*, facilitating precision measurements of structure growth and tests of gravity. All codes and trained emulators are publicly available in the `freyja` repository. 

**Key words:** dark energy – large-scale structure of Universe – cosmology: miscellaneous – cosmology: theory.

## 1 INTRODUCTION

The present decade marks a golden era for extragalactic astronomy and cosmology. Large-scale structure (LSS) surveys, such as the Dark Energy Spectroscopic Instrument (DESI) (DESI Collaboration et al. 2016) and the *Euclid* mission (Laureijs et al. 2011; Amendola et al. 2013; Euclid Collaboration et al. 2025), have begun to map the distribution of millions of galaxies over vast cosmic volumes. To fully exploit the statistical power of these surveys, theoretical predictions must match the sub-percent precision of the observational data. A key probe for extracting cosmological information from spectroscopic surveys is redshift-space distortions of clustering (Kaiser 1987). The peculiar velocities of galaxies, mainly induced by the gravity of the inhomogeneous matter distribution, introduce an anisotropy in the observed clustering signal along the line of sight. This effect breaks the degeneracy between the galaxy

bias and the growth rate of structure,  $f$ , making RSD a powerful tool for probing the growth history of the Universe (e.g. Peacock et al. 2001; Hawkins et al. 2003; Cole et al. 2005; Guzzo et al. 2008).

The streaming model (Peebles 1980; Davis & Peebles 1983; Fisher 1995; Scoccimarro 2004; Kuruvilla & Porciani 2018) provides an accurate way of describing the RSD effect by decomposing the redshift-space clustering,  $\xi^S(s_\perp, s_\parallel)$ , into two distinct ingredients: the real-space clustering of galaxies,  $\xi^R(r)$ , which encodes their spatial distribution, and the velocity information encoded by the pairwise line-of-sight velocity distribution  $\mathcal{P}(v_\parallel)$ . As a result, the streaming model offers a clear physical interpretation of RSD and a convenient bridge between theoretical models, numerical simulations, and observational measurements.

The halo model (Seljak 2000; Cooray & Sheth 2002; Schmidt 2016; Asgari et al. 2023), combined with the halo occupation distribution (HOD) framework (Benson et al. 2000; Zheng 2004; Kravtsov et al. 2004), provides a systematic and physically motivated description of galaxy clustering by connecting galaxies to their host dark matter haloes. It has been widely used to constrain cosmolo-

\* E-mail: cheng-zong.ruan@durham.ac.uk

† E-mail: baojiu.li@durham.ac.uk

gical and galaxy-halo connection parameters (e.g. Tinker et al. 2005; van den Bosch et al. 2013; Mead & Verde 2021; Mahony et al. 2022; Dvornik et al. 2023). In this approach, the full galaxy two-point correlation function is decomposed according to both galaxy type and halo environment. Galaxies are classified as centrals, residing at the centres of haloes, or satellites, orbiting within haloes. Galaxy pairs are further separated into intra-halo and inter-halo contributions. This leads to a natural decomposition of the galaxy clustering signal into 1-halo and 2-halo terms, and each term receives contributions from central-central, central-satellite, and satellite-satellite pairs (see e.g. Zheng et al. 2005), allowing different physical processes to be modelled in a modular and tailored way.

The unified *halo streaming model* proposed here integrates the halo- and streaming-model formalisms to decompose the redshift-space clustering signal into fundamental building blocks, following Tinker (2007) (see also Zheng & Guo 2016 and Nishimichi et al. 2019). The halo model expresses the real-space galaxy clustering and velocity statistics as a sum of contributions from different galaxy types and halo configurations. The streaming model then maps each real-space component to redshift space. This framework reduces the complexity of nonlinear redshift-space clustering to a collection of basic ingredients that can be modelled, calibrated, or emulated independently, providing a transparent and modular pathway from theoretical assumptions to observable galaxy clustering signals.

In recent years, the demand for precision has driven the field toward simulation-based approaches and emulators (e.g. Heitmann et al. 2010; DeRose et al. 2019; Zhai et al. 2019; Miyatake et al. 2020; Maksimova et al. 2021; Cuesta-Lazaro et al. 2024; Paillas et al. 2024). After being trained using  $N$ -body simulations, emulators can predict halo and galaxy clustering statistics with a high accuracy. Directly emulating the full redshift-space signal, however, results in a high-dimensional “black box” that can lack physical transparency and may struggle to generalise across different tracer populations or extensions to the cosmological model.

The halo streaming model is a unified framework that combines the physical interpretability of analytical models with the accuracy of emulation. We adopt a *modular ‘emulation* strategy, modernizing the philosophy based on Tinker (2007): rather than relying on fitting functions for the model ingredients, we train emulators for the building blocks, including the halo mass function, the real-space halo-halo correlation function, and the pairwise velocity moments. This work extends Cuesta-Lazaro et al. (2023), which focuses on emulating the real-space clustering of haloes and combining this with a halo-model/HOD prescription, by providing the additional ingredients required by the streaming model, enabling direct predictions of the full anisotropic redshift-space clustering signal.

This paper is organised as follows. Section 2 describes the suite of  $N$ -body simulations used in this work. In Section 3, we review the formalism of the halo streaming model and the decomposition of the galaxy correlation function. Section 4 presents the construction and tests of the emulators for the halo model ingredients. Section 5 demonstrates that the model can accurately recover the cosmological parameters with mock galaxy observations. Finally, we discuss the implications for future surveys and conclude in Section 6. The code developed for this work, including the trained emulators, is made publicly available via the `freyja` repository<sup>1</sup>.

## 2 SIMULATIONS AND MOCK CATALOGUES

### 2.1 The DEGRACE-pilot simulation suite

To construct the ingredients of the halo streaming model and train the emulators, we make use of a new suite of  $N$ -body simulations, hereafter referred to as DEGRACE<sup>2</sup>-pilot. It comprises 64  $\Lambda$ CDM models that span a four-dimensional cosmological parameter space,

$$\mathcal{C} = \left\{ \Omega_{\text{m}0}, h, S_8, n_s \right\}, \quad (1)$$

where  $h \equiv H_0 / (100 \text{ km s}^{-1} \text{ Mpc}^{-1})$  with  $H_0$  being the Hubble constant;  $S_8 \equiv \sigma_8 \sqrt{\Omega_{\text{m}0} / 0.3}$  characterises the amplitude of matter fluctuations;  $\Omega_{\text{m}0}$  is the (baryonic plus cold dark) matter density parameter today; and  $n_s$  denotes the spectral index of the primordial power spectrum. For each cosmological model, we generate five independent realisations in order to suppress sample variance. We employ a Sobol sequence (Sobol 1967; Matoušek 1998) to sample the parameter values, providing an efficient and statistically uniform coverage of the multidimensional space, as illustrated in Fig. 1. The Sobol design is similar to Latin hypercube sampling, but further allows for straightforward extensions of the sampling. The parameter ranges explored are

$$\begin{aligned} 0.15 < \Omega_{\text{m}0} < 0.45, \\ 0.60 < h < 0.80, \\ 0.65 < S_8 < 0.95, \\ 0.94 < n_s < 0.99. \end{aligned} \quad (2)$$

The physical baryonic and neutrino densities are fixed to  $\Omega_{\text{b}0} h^2 = 0.0224$  and  $\Omega_{\nu} h^2 = 0.00064$ , respectively, corresponding to a total neutrino mass of 0.06 eV. Assuming spatial flatness, the dark energy density parameter is given by  $\Omega_{\Lambda 0} = 1 - \Omega_{\text{m}0}$ . In addition to  $\Lambda$ CDM, we have also generated suites of modified-gravity simulations based on  $f(R)$  and DGP models; however, the present work focuses exclusively on the standard cosmological model, leaving the analysis of the MG runs to future studies.

All simulations were performed with the GLAM code (Klypin & Prada 2018; Klypin et al. 2021), a particle-mesh  $N$ -body solver optimised for large ensembles of simulations. GLAM employs OPENMP-based shared-memory parallelism, allowing many independent realisations to be run across multiple compute nodes. Combined with its fixed force and mass resolutions, this design makes GLAM particularly well suited for large emulator campaigns that require a high throughput of simulations spanning a wide range of cosmological models. Its speed and scalability enable the efficient production of halo catalogues and mock galaxy samples, which form the essential training data for emulator construction.

Each run evolves  $N_p = 2048^3$  particles within a cubic volume of side length  $L = 1024 h^{-1} \text{ Mpc}$ . The gravitational potential is computed on a mesh of  $N_g = 4096^3$  cells, corresponding to a spatial resolution of  $0.25 h^{-1} \text{ Mpc}$ . This translates to a minimum reliably resolved halo mass of  $10^{12.4} h^{-1} M_{\odot}$  at redshift  $z = 0.25$  for  $\Omega_{\text{m}0} \approx 0.3$  (cf. Hernández-Aguayo et al. 2021; Ruan et al. 2022b). The simulation configuration provides a good compromise between large volume (required for capturing long-wavelength modes and suppressing sample variance) and sufficient mass resolution to resolve dark matter haloes hosting galaxies targeted by ongoing and forthcoming surveys.

<sup>2</sup> Abbreviation for Dark Energy, GRavity and the Accelerated Cosmic Expansion.

<sup>1</sup> <https://github.com/chzruan/freyja>

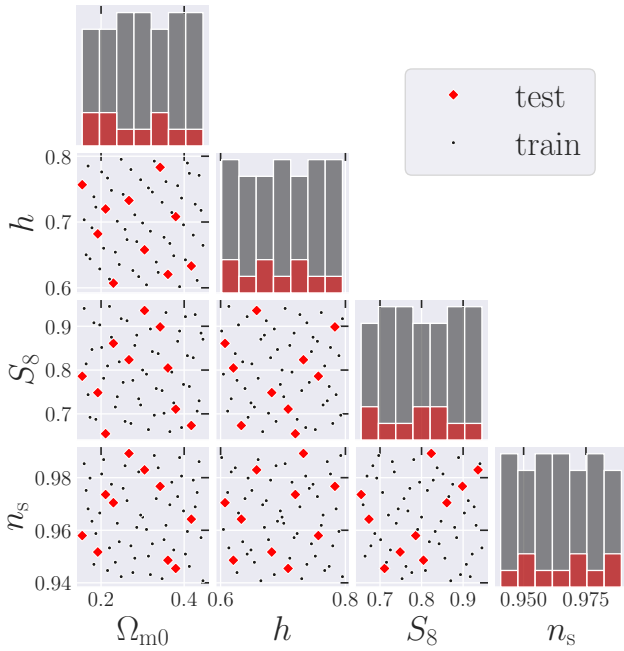


**Figure 1.** Visualisation of the cosmological parameter space,  $\mathcal{C}$ , covered by the DEGRACE-pilot simulation suite. The suite includes 64 cosmological models, of which models 1-54 are used for training and 55-64 are reserved for testing. 

## 2.2 HOD prescriptions

The halo streaming model can be combined with arbitrary halo occupation distribution prescriptions to model galaxy clustering. In this work, we adopt a standard HOD parameterisation as a baseline to test and validate our model pipeline.

Galaxy populations are assigned to dark matter haloes using the conventional HOD framework (Berlind et al. 2003; Zheng et al. 2005). The free parameters of the model are

$$\mathcal{G} = \left\{ \log M_{\text{cut}}, \log M_1, \alpha, \sigma, \alpha_c^{\text{vel}}, \alpha_s^{\text{vel}} \right\}, \quad (3)$$

where  $\log M_{\text{cut}}$  and  $\sigma$  control the abundance of central galaxies,  $\log M_1$  and  $\alpha$  describe the satellite occupation, and  $\alpha_c^{\text{vel}}$  and  $\alpha_s^{\text{vel}}$  are velocity bias parameters for centrals and satellites, respectively. The parameter  $\kappa$ , which shifts the minimum mass scale for satellite occupation, is fixed to unity since it has a negligible impact on the clustering statistics considered here.

The mean numbers of central and satellite galaxies hosted by a halo of mass  $M$  are specified as

$$\langle N_c \rangle(M) = \frac{1}{2} \left[ 1 + \text{erf} \left( \frac{\log M - \log M_{\text{cut}}}{\sqrt{2} \sigma} \right) \right], \quad (4)$$

$$\langle N_s \rangle(M) = \langle N_c \rangle(M) \left( \frac{M - \kappa M_{\text{cut}}}{M_1} \right)^\alpha, \quad (5)$$

where  $\langle N_c \rangle(M)$  transitions smoothly from 0 to 1, while  $\langle N_s \rangle$  scales as a power law above the mass threshold  $\kappa M_{\text{cut}}$ . Central galaxies are placed at the centres of their host haloes. Satellite galaxies are distributed radially according to the host halo density profile, with isotropic angular positions.

The velocity of each galaxy is given by the halo bulk velocity

plus a stochastic component along the Cartesian coordinates:

$$\mathbf{v}_c = \mathbf{v}_h + \mathbf{v}_{c,\text{sto}}, \quad (6)$$

$$\mathbf{v}_s = \mathbf{v}_h + \mathbf{v}_{s,\text{sto}}, \quad (7)$$

where the stochastic terms are drawn from independent Gaussian distributions,

$$v_{c/s,\text{sto}}^{x/y/z} \sim \mathcal{N}(0, \alpha_{c/s}^2 \sigma_{\text{vir}}^2(M_h)). \quad (8)$$

Here  $\sigma_{\text{vir}}(M_h)$  denotes the halo virial velocity dispersion, measured directly from simulations or approximated as

$$\sigma_{\text{vir}}(M_h) \equiv \sqrt{\frac{GM_h}{2R_h}}. \quad (9)$$

The velocity bias parameters  $\alpha_c^{\text{vel}}$  and  $\alpha_s^{\text{vel}}$  allow for deviations from this virial expectation and are therefore essential for accurately modelling redshift-space clustering. While a variety of galaxy-halo connection prescriptions have been explored in the literature (e.g. Zheng et al. 2005, 2007), our implementation places particular emphasis on the velocity assignment scheme. This choice directly determines the line-of-sight pairwise velocity distributions of galaxies, which in turn control the fidelity of RSD modelling within the streaming framework.

## 2.3 HOD Variants and Extensions

A wide range of extensions to the standard halo occupation distribution framework have been proposed to capture increasingly complex aspects of the galaxy-halo connection. These include models incorporating galaxy assembly bias, where galaxy occupation depends on secondary halo properties other than mass, as well as alternative formulations such as the conditional luminosity or stellar mass functions. More recent approaches combine empirical and physical modelling, for example through subhalo abundance matching (SHAM, Conroy et al. 2006) or hybrid HOD-SHAM schemes. While such variants can reproduce specific observational features with high fidelity, they typically introduce additional free parameters and degeneracies that complicate parameter inference and model calibration.

Here, we deliberately adopt a minimal, mass-only HOD based on the standard parameterisation (Zheng et al. 2005), without assembly bias (Hearin et al. 2016). Satellite occupations are assumed to follow Poisson statistics, galaxy positions trace spherical NFW profiles, and galaxy velocities are modelled with Gaussian stochastic components augmented by central and satellite velocity bias parameters. This baseline choice is sufficient for testing the halo streaming framework and emulator pipeline developed here, while maintaining a clear separation between cosmological and astrophysical degrees of freedom. A more comprehensive exploration of extended HOD prescriptions is beyond the scope of this work.

## 3 THE HALO STREAMING MODEL OF REDSHIFT-SPACE CLUSTERING

### 3.1 The streaming model for RSD

Within the halo model framework, the galaxy-galaxy two-point correlation function,  $\xi_{\text{gg}}$ , can be decomposed into its constituent one-halo and two-halo terms. This decomposition is valid in both real and redshift space and is given by:

$$\xi_{\text{gg}} = f_c^2 \xi_{\text{cc}}^{2\text{h}} + 2f_c f_s \left( \xi_{\text{cs}}^{1\text{h}} + \xi_{\text{cs}}^{2\text{h}} \right) + f_s^2 \left( \xi_{\text{ss}}^{1\text{h}} + \xi_{\text{ss}}^{2\text{h}} \right), \quad (10)$$

where  $f_c \equiv n_c/n_g$  and  $f_s \equiv n_s/n_g$  are the number fractions of central and satellite galaxies, respectively, and  $n_c$ ,  $n_s$  and  $n_g$  are the numbers of central, satellite and all galaxies.

To model RSD, we need to consider the kinematics of galaxy pairs. For a pair of tracer galaxies with real-space positions  $\mathbf{r}_1, \mathbf{r}_2$  and peculiar velocities  $\mathbf{v}_1, \mathbf{v}_2$ , their separation vector is  $\mathbf{r} \equiv \mathbf{r}_2 - \mathbf{r}_1$  and their pairwise peculiar velocity is  $\mathbf{v} \equiv \mathbf{v}_2 - \mathbf{v}_1$ . The redshift-space clustering is distorted by the component of the pairwise velocity along the line-of-sight (LOS). To describe this effect, we adopt a coordinate system in which the LOS direction  $\hat{\ell}$  is fixed along the  $z$ -axis under the plane-parallel approximation, i.e.,  $\hat{\ell} \approx \hat{z}$ . It is useful to decompose the pairwise velocity  $\mathbf{v}$  into components that are radial ( $v_r$ ) and transverse ( $v_t$ ) with respect to the pair separation vector  $\mathbf{r}$ . These components are defined by projecting  $\mathbf{v}$  onto the unit vectors:

$$\hat{\mathbf{r}} \equiv \mathbf{r}/r, \quad \hat{\mathbf{t}} \equiv \hat{\mathbf{r}} \times \hat{\ell} \approx \hat{\mathbf{r}} \times \hat{z}. \quad (11)$$

The radial, transverse, and LOS components of the pairwise velocity are then related by:

$$v_r = \mathbf{v} \cdot \hat{\mathbf{r}}, \quad v_t = \mathbf{v} \cdot \hat{\mathbf{t}}, \quad (12)$$

$$v_{\parallel} = \mathbf{v} \cdot \hat{\ell} = v_r \cos \theta + v_t \sin \theta, \quad (13)$$

where  $\theta$  is the angle between the separation vector  $\mathbf{r} = (r_{\perp}, r_{\parallel})$  and the LOS direction.

The LOS peculiar velocity distorts the observed separation of the galaxy pair. The mapping from the real-space separation vector  $\mathbf{r}$  to the redshift-space separation vector  $\mathbf{s}$  is given by:

$$\mathbf{s} = \mathbf{r} + \frac{v_{\parallel}}{aH(a)} \hat{z}, \quad (14)$$

where  $a$  is the scale factor and  $H(a)$  is the Hubble parameter. This mapping forms the basis of the streaming model (e.g. Peebles 1980; Fisher 1995; Scoccimarro 2004; Kuruvilla & Porciani 2018, 2020), which relates the redshift-space 2PCF,  $\xi^S(s_{\perp}, s_{\parallel})$ , to its real-space counterpart,  $\xi^R(r)$ :

$$1 + \xi^S(s_{\perp}, s_{\parallel}) = \int_{-\infty}^{\infty} dr_{\parallel} \left[ 1 + \xi^R(r) \right] \mathcal{P}(v_{\parallel} | r_{\perp}, r_{\parallel}). \quad (15)$$

In this equation, the respective separation components are related by  $v_{\parallel} = (s_{\parallel} - r_{\parallel})/(aH)$ ,  $r_{\perp} = s_{\perp}$ , and  $r = \sqrt{r_{\perp}^2 + r_{\parallel}^2}$ . The kernel of the integral,  $\mathcal{P}(v_{\parallel} | \mathbf{r})$ , is the probability distribution function (PDF) of the pairwise LOS velocity for a given real-space separation  $\mathbf{r} = (r_{\perp}, r_{\parallel})$ .

The main idea here is to use the halo model together with the HOD framework to explicitly separate galaxy pairs into one-halo (pairs within the same halo) and two-halo (pairs in different haloes) components, as well as into central-central, central-satellite, and satellite-satellite pair types:

$$\xi_{\text{gg}}^S(s_{\perp}, s_{\parallel}) \xrightarrow{\text{halo model}} \begin{cases} \xi_{\text{cs}}^{\text{S,1h}}(r), \xi_{\text{ss}}^{\text{S,1h}}(r) \\ \xi_{\text{cc}}^{\text{S,2h}}(r), \xi_{\text{cs}}^{\text{S,2h}}(r), \xi_{\text{ss}}^{\text{S,2h}}(r). \end{cases} \quad (16)$$

We then apply the streaming model to each pair type separately, so that the redshift-space 2PCF can be expressed in terms of its real-space clustering and pairwise velocity distribution components,

$$\xi_{\text{cc}}^{\text{S,2h}}(s_{\perp}, s_{\parallel}) \xrightarrow{\text{streaming model}} \begin{cases} \xi_{\text{cc}}^{\text{R,2h}}(r), \\ \mathcal{P}_{\text{cc}}^{\text{2h}}(v_{\parallel} | \mathbf{r}). \end{cases} \quad (17)$$

### 3.2 One-halo terms

In this section, we present the analytical expressions for the one-halo terms of the 2PCF, which describe the correlation of galaxy pairs

residing within the same dark matter halo. The real-space one-halo terms for central-satellite (cs) and satellite-satellite (ss) pairs are given by:

$$\xi_{\text{cs}}^{\text{R,1h}}(r) \equiv \frac{1}{n_c n_s} \int dM \frac{dn(M)}{dM} \langle N_c N_s \rangle(M) u_s(r|M), \quad (18)$$

$$\xi_{\text{ss}}^{\text{R,1h}}(r) = \frac{1}{n_s^2} \int dM \frac{dn(M)}{dM} \langle N_s(N_s - 1) \rangle(M) \lambda_{\text{ss}}(r|M). \quad (19)$$

Here,  $dn/dM$  is the halo mass function. The term  $u_s(r|M)$  is the normalised radial number density profile of satellite galaxies within a halo of mass  $M$ . The term  $\lambda_{\text{ss}}(r|M)$  is the auto-convolution of the satellite profile:

$$\lambda_{\text{ss}}(r|M) \equiv \int d\mathbf{x} u_s(\mathbf{x}|M) u_s(\mathbf{x} + \mathbf{r}|M). \quad (20)$$

The terms  $\langle N_c N_s \rangle(M)$  and  $\langle N_s(N_s - 1) \rangle(M)$  are the first and second factorial moments of the HOD, representing the average number of central-satellite pairs and satellite-satellite pairs, respectively. We adopt the standard HOD prescription for luminous red galaxies: a halo hosts at most one central galaxy, and the number of satellites,  $N_s$ , follows a Poisson distribution. Under these assumptions, these terms simplify to (cf. Equations (4)-(6) of Zheng et al. 2005):

$$\langle N_c N_s \rangle(M) = \langle N_s \rangle(M) \quad (21)$$

$$\langle N_s(N_s - 1) \rangle(M) = [\langle N_s \rangle(M)]^2. \quad (22)$$

To model the one-halo term in redshift space, we must account for the internal (virial) motions of galaxies within haloes. For a galaxy pair in the same halo, the bulk velocity of the halo cancels out, and their relative peculiar velocity is determined by their orbits. Following the velocity assignment scheme in Section 2.2, we model the pairwise LOS velocity distributions,  $\mathcal{P}(v_{\parallel})$ , as Gaussians with zero mean. The variances depend on the halo velocity dispersion,  $\sigma(M)$ , and the velocity bias parameters,  $\alpha^{\text{vel}}$ :

$$\mathcal{P}_{\text{cs}}^{\text{1h}}(v_{\parallel} | M) \sim \mathcal{N} \left[ 0, \left( \alpha_c^{\text{vel}} \sigma(M) \right)^2 + \left( \alpha_s^{\text{vel}} \sigma(M) \right)^2 \right] \quad (23)$$

$$\mathcal{P}_{\text{ss}}^{\text{1h}}(v_{\parallel} | M) \sim \mathcal{N} \left[ 0, \left( \sqrt{2} \alpha_s^{\text{vel}} \sigma(M) \right)^2 \right], \quad (24)$$

where  $\mathcal{N}[\mu, \sigma^2]$  denotes a Gaussian distribution with mean  $\mu$  and variance  $\sigma^2$ .

Applying the streaming model of Section 3.1, we convolve the real-space profiles with these velocity PDFs to obtain the redshift-space one-halo terms:

$$1 + \xi_{\text{cs}}^{\text{S,1h}}(s_{\perp}, s_{\parallel}) = \frac{1}{n_c n_s} \int dM \frac{dn(M)}{dM} \langle N_s \rangle(M) \dots \int dr_{\parallel} u_s(r|M) \mathcal{P}_{\text{cs}}^{\text{1h}}(s_{\parallel} - r_{\parallel} | M), \quad (25)$$

$$1 + \xi_{\text{ss}}^{\text{S,1h}}(s_{\perp}, s_{\parallel}) = \frac{1}{n_s^2} \int dM \frac{dn(M)}{dM} [\langle N_s \rangle(M)]^2 \dots \int dr_{\parallel} \lambda_{\text{ss}}(r|M) \mathcal{P}_{\text{ss}}^{\text{1h}}(s_{\parallel} - r_{\parallel} | M), \quad (26)$$

and calculate the convolution integral for the satellite-satellite term using the convolution theorem:

$$\lambda_{\text{ss}}(r|M) = \mathcal{F}^{-1} \left\{ [\tilde{u}_s(k|M)]^2 \right\} (r), \quad (27)$$

where  $\tilde{u}_s(k|M)$  is the Fourier transform of  $u_s(x|M)$  and  $\mathcal{F}^{-1}$  denotes the inverse Fourier transform.

### 3.3 Two-halo terms

The two-halo term, which accounts for the correlation between galaxies in different haloes, dominates the 2PCF on scales  $r \gtrsim 2\text{--}3 h^{-1}\text{Mpc}$ . We decompose redshift-space 2-halo terms using the streaming model:

$$1 + \xi_{\text{ab}}^{\text{S,2h}}(s_{\perp}, s_{\parallel}) = \int_{-\infty}^{\infty} dr_{\parallel} \left[ 1 + \xi_{\text{ab}}^{\text{R,2h}}(r) \right] \mathcal{P}_{\text{ab}}^{\text{2h}}(v_{\parallel}|\mathbf{r}), \quad (28)$$

where  $\text{ab} = \{\text{cc}, \text{cs}, \text{ss}\}$ . This expression requires models for both the real-space two-halo term,  $\xi_{\text{ab}}^{\text{R,2h}}(r)$ , and the two-halo pairwise velocity PDF,  $\mathcal{P}^{\text{2h}}$ .

In the halo model framework, the central-central term can be written as

$$\xi_{\text{cc}}^{\text{R,2h}}(r) = \frac{1}{n_c^2} \int dM_1 \frac{dn(M_1)}{dM_1} \langle N_c(M_1) \rangle \dots \int dM_2 \frac{dn(M_2)}{dM_2} \langle N_c(M_2) \rangle \xi_{\text{hh}}^{\text{R}}(r|M_1, M_2). \quad (29)$$

The terms involving satellite galaxies will contain convolutions between halo 2PCFs and satellite profiles. It is simpler to compute them in Fourier space, in which convolutions become products of Fourier modes, then inverse transform back to configuration space (Cuesta-Lazaro et al. 2023),

$$P_{\text{cs}}^{\text{R,2h}}(k) = \frac{1}{n_c n_s} \int dM_1 \frac{dn(M_1)}{dM_1} \langle N_c(M_1) \rangle \dots \int dM_2 \frac{dn(M_2)}{dM_2} \langle N_s(M_2) \rangle \dots P_{\text{hh}}(k|M_1, M_2) u_s(k|M_2), \quad (30)$$

$$P_{\text{ss}}^{\text{R,2h}}(k) = \frac{1}{n_s^2} \int dM_1 \frac{dn(M_1)}{dM_1} \langle N_s(M_1) \rangle \dots \int dM_2 \frac{dn(M_2)}{dM_2} \langle N_s(M_2) \rangle \dots P_{\text{hh}}(k|M_1, M_2) u_s(k|M_1) u_s(k|M_2), \quad (31)$$

Now we turn to the line-of-sight pairwise velocity distributions of the 2-halo terms  $\mathcal{P}_{\text{ab}}^{\text{2h}}(v_{\parallel}|\mathbf{r})$ . Following the same spirit of maximally exploiting the statistical symmetry in real-space, we choose to model the joint distribution of radial-transverse pairwise velocities,  $\mathcal{P}_{\text{ab}}^{\text{2h}}(v_r, v_t|r \equiv |\mathbf{r}|)$ , then project it to the line-of-sight direction. As in previous works (Cuesta-Lazaro et al. 2020; Ruan et al. 2022a), we adopt the skew-T distribution to incorporate the beyond-Gaussian properties of the pairwise velocity distributions, which will be detailed in the following subsection.

### 3.4 The skew-T parameterisation of the pairwise velocity distribution

An accurate model for the pairwise velocity probability distribution function is essential for applying the streaming model. Following recent advancements in the field, we adopt the flexible, four-parameter skewed Student's t-distribution (hereafter ST distribution) proposed by Azzalini & Capitanio (2009); Zu & Weinberg (2013); Cuesta-Lazaro et al. (2020). A key advantage of this model is that its four parameters are uniquely determined by the first four moments of the distribution: the mean, variance, skewness, and kurtosis. This allows the model to capture the non-Gaussian features of the pairwise velocity field robustly.

While the LOS pairwise velocity,  $v_{\parallel}$ , is the observable quantity, the underlying physics is more naturally described by the joint

PDF of the velocity components parallel (radial,  $v_r$ ) and perpendicular (transverse,  $v_t$ ) to the pair separation vector, defined in Equation (13). Due to statistical isotropy in real space, this joint PDF,  $\mathcal{P}(v_r, v_t|r)$ , depends only on the separation magnitude  $r$ . The LOS velocity PDF,  $\mathcal{P}(v_{\parallel}|\mathbf{r})$ , is a projection of this fundamental 2D distribution that depends on the orientation of the pair separation  $\mathbf{r}$  with respect to the LOS. The relationship between the two, derived from Equation (13), is:

$$\mathcal{P}(v_{\parallel}|\mathbf{r}) = \int \frac{dv_r}{\sin \theta} \mathcal{P}\left(v_r, v_t = \frac{v_{\parallel} - v_r \cos \theta}{\sin \theta} \middle| r\right). \quad (32)$$

A PDF can be characterised via its moments. For the 2D joint distribution  $\mathcal{P}(v_r, v_t|r)$ , the raw moments  $m_{ij}$  and central moments  $c_{ij}$  are defined as:

$$\begin{cases} m_{ij}(r) \equiv \iint dv_r dv_t (v_r)^i (v_t)^j \mathcal{P}(v_r, v_t|r), \\ c_{ij}(r) \equiv \iint dv_r dv_t [v_r - m_{10}(r)]^i [v_t - m_{01}(r)]^j \mathcal{P}(v_r, v_t|r). \end{cases} \quad (33)$$

Due to statistical isotropy, the system is symmetric in the transverse direction, which implies that all moments with an odd power  $j$  of the transverse velocity component are zero (e.g.  $m_{01}$ ,  $c_{21}$  and  $c_{03}$ ).

Similarly, the  $n$ -th order raw ( $m_n$ ) and central ( $c_n$ ) moments of the 1D LOS velocity distribution are:

$$\begin{cases} m_n(\mathbf{r}) \equiv \int dv_{\parallel} (v_{\parallel})^n \mathcal{P}(v_{\parallel}|r_{\perp}, r_{\parallel}), \\ c_n(\mathbf{r}) \equiv \int dv_{\parallel} [v_{\parallel} - m_1(\mathbf{r})]^n \mathcal{P}(v_{\parallel}|r_{\perp}, r_{\parallel}). \end{cases} \quad (34)$$

The moments of the 1D LOS distribution can be expressed analytically in terms of the moments of the underlying 2D distribution. Up to the fourth order, these projection relations are:

$$\begin{cases} m_1(\mathbf{r}) = \mu m_{10}(r) \\ c_2(\mathbf{r}) = (1 - \mu^2)c_{02}(r) + \mu^2 c_{20}(r) \\ c_3(\mathbf{r}) = 3\mu(1 - \mu^2)c_{12}(r) + \mu^3 c_{30}(r) \\ c_4(\mathbf{r}) = (1 - \mu^2)^2 c_{04}(r) + 6\mu^2(1 - \mu^2)c_{22}(r) + \mu^4 c_{40}(r), \end{cases} \quad (35)$$

where  $\mu \equiv \cos \theta = r_{\parallel}/r$ , with  $\theta$  introduced below Eq. (13). This set of equations allows us to calculate the anisotropic LOS moments from the isotropic radial/transverse moments.

This provides a useful strategy for reducing the sample variances of the velocity moments from simulations. Instead of directly measuring angle-dependent (and thus noisier) LOS moments  $c_n(\mathbf{r})$ , we first measure the simpler isotropic moments of the 2D distribution, which are functions of  $r$  only:

$$\begin{cases} m_{10}(r), \\ c_{02}(r), c_{20}(r), \\ c_{12}(r), c_{30}(r), \\ c_{04}(r), c_{22}(r), c_{40}(r). \end{cases} \quad (36)$$

By averaging over all pair orientations at a fixed separation  $r$ , we can obtain high-precision measurements of these fundamental moments. We then use Equation (35) to analytically project these moments and construct the required LOS velocity moments for any orientation  $\mathbf{r}$ .

With the first four LOS moments ( $m_1, c_2, c_3, c_4$ ) in hand, we

reconstruct the full velocity PDF using the ST distribution:

$$\mathcal{P}_{\text{los}}^{\text{ST}}(v_{\parallel}|v_c(\mathbf{r}), w(\mathbf{r}), \alpha(\mathbf{r}), \nu(\mathbf{r})) = \frac{2}{w} t(v_{\parallel} - v_c; \nu) \times T\left(\alpha \frac{v_{\parallel} - v_c}{w} \left[ \frac{\nu + 1}{\nu + ((v_{\parallel} - v_c)/w)^2} \right]^{1/2}; \nu + 1\right), \quad (37)$$

where  $t(x; \nu)$  is the Student's  $t$ -distribution with  $\nu$  degrees of freedom, and  $T(x; \nu + 1)$  is its cumulative distribution function with the number of degrees of freedom  $\nu + 1$ . The four parameters of the ST distribution — location  $v_c(\mathbf{r})$ , scale  $w(\mathbf{r})$ , skewness  $\alpha(\mathbf{r})$ , and tail-weight  $\nu(\mathbf{r})$  — are uniquely determined by the four LOS moments we constructed, see Equations (A1)–(A6) in appendix A of [Cuesta-Lazaro et al. \(2020\)](#).

#### 4 EMULATORS FOR THE MODEL INGREDIENTS

The halo streaming model developed here relies on several physical ingredients, such as the halo abundance, clustering, and velocity statistics. Directly measuring these quantities from simulations during parameter inference would be computationally prohibitive. We therefore construct a suite of emulators that provide fast and accurate predictions across cosmologies, halo mass, and scale. Each emulator targets a reduced or physically normalised quantity chosen to minimise dynamic range, improve smoothness, and enforce correct large-scale behaviour. Gaussian-process (GP, [Williams & Rasmussen 2006](#)) models are adopted for smooth, low-dimensional functions, while neural networks (NNs, [Bishop et al. 1995](#); [Alom et al. 2019](#); [Zhang et al. 2021](#)) are used for higher-dimensional quantities with strong scale dependence. Table 1 summarises the emulated quantities, their physical definitions, and the surrogate models employed.

##### 4.1 Halo mass functions

We construct an emulator for the cumulative halo mass function (HMF) using GP regression. This allows us to predict the abundance of haloes as a continuous function of both cosmological parameters and halo mass.

###### 4.1.1 Training Data and Input Space

The training data consist of  $N_{\text{train}} = 54$  cosmological models from the simulation suite. For each model, we utilise the halo mass function measured in discrete mass bins. To ensure the stability of the emulator in the high-mass tail where shot noise is dominant, we restrict the training data to mass scales of  $\log_{10}(M[M_{\odot}/h]) \leq 14.8$  at redshift  $z = 0.25$ . The cHMFs above the threshold mass bin are modelled separately using analytic Schechter-like fits to suppress high-mass noise, as will be described in Section 4.1.3.

We opt to construct a single global emulator over the joint input space of cosmology and halo mass. The input vector  $\mathbf{x}$  is defined as a five-dimensional vector:

$$\mathbf{x} = \{\Omega_{\text{m}0}, h, S_8, n_s, \log_{10} M\}. \quad (38)$$

By treating the halo mass as an input dimension, the GP can exploit correlations between mass bins, effectively smoothing the predictions and providing a continuous derivative with respect to mass.

To reduce the dynamic range of the target function and improve the performance of the GP, we emulate the *ratio* of the measured

simulation HMF to a theoretical reference model, rather than the number density directly. The target variable  $y$  is given by:

$$y(\mathbf{x}) = \frac{n_{\text{sim}}(> M|\mathcal{C})}{n_{\text{ref}}(> M|\mathcal{C})}. \quad (39)$$

The reference cumulative HMF,  $n_{\text{ref}}(> M)$ , is calculated using the Sheth-Mo-Tormen mass function ([Sheth et al. 2001](#)) as implemented in the `hmf` Python package ([Murray et al. 2013, 2021](#)).

###### 4.1.2 Gaussian Process Implementation

We model the target function  $y(\mathbf{x})$  as a Gaussian Process,

$$y(\mathbf{x}) \sim \mathcal{GP}[\mu(\mathbf{x}), k(\mathbf{x}, \mathbf{x}')]. \quad (40)$$

The covariance between any two points in the five-dimensional input space is modelled using an anisotropic radial basis function (RBF), also known as the squared exponential kernel:

$$k(\mathbf{x}_i, \mathbf{x}_j) = A \exp\left(-\frac{1}{2} \sum_{d=1}^5 \frac{(x_{i,d} - x_{j,d})^2}{\ell_d^2}\right) + \delta_{ij} \sigma_n^2, \quad (41)$$

where  $A$  is the signal amplitude,  $\ell_d$  are the characteristic length-scales for each of the five input dimensions of  $\mathbf{x}$  defined in Equation (38), and  $\delta_{ij} \sigma_n^2$  represents a fixed noise (jitter) term added to the diagonal for numerical stability, set to  $\sigma_n^2 = 10^{-5}$ . We use the `tinygp` package ([Foreman-Mackey et al. 2024](#)) for efficient GP implementation. The kernel hyper-parameters  $\phi = \{A, \ell_1, \dots, \ell_5\}$  are determined by maximising the log-marginal likelihood of the training data:

$$\ln \mathcal{L}(\phi) = -\frac{1}{2} \mathbf{y}^{\top} \mathbf{K}^{-1} \mathbf{y} - \frac{1}{2} \ln |\mathbf{K}| + \text{const.}, \quad (42)$$

where  $\mathbf{y}$  is the vector of training targets across all simulations and mass bins,  $N = N_{\text{model}} \times N_{\text{mass bins}}$  is the total number of training points and  $\mathbf{K}$  is the  $N \times N$  covariance matrix, with entries  $K_{ij} = k(\mathbf{x}_i, \mathbf{x}_j)$ . Optimisation is performed using the `Optax` library ([DeepMind et al. 2020](#)). We use a learning rate of  $\eta = 0.05$  and train for 500 iterations to ensure convergence of the hyper-parameters.

###### 4.1.3 The high-mass tail of halo mass functions

Direct measurements of the halo mass function from simulations suffer from significant shot noise at the high-mass end where halo number counts are small. To address this problem, we adopt a two-step strategy that prioritises emulation accuracy.

First, we train our emulators exclusively within the mass range  $10^{12.4} \leq [M/(h^{-1} M_{\odot})] \leq 10^{14.7}$ , where the lower limit is dictated by the simulation mass resolution, and the upper limit corresponds to a minimum threshold of  $N_{\text{thre}} = 100$  halos in the cumulative mass bin. By restricting the training data to this well-sampled regime, we ensure high fidelity in the emulation. Second, to extend the higher mass range of HMF predictions, we fit a generalised Schechter function to the high-precision emulated HMFs obtained in the first step and extrapolate this parametric form to higher masses. The parametric form used is:

$$n(> M) = \phi_{\star} \left(\frac{M}{M_1}\right)^{-\alpha} \exp\left[-\left(\frac{M}{M_2}\right)^{\beta}\right], \quad (43)$$

where  $\phi_{\star}$  is the normalisation constant,  $M_1$  and  $M_2$  control the characteristic mass scales,  $\alpha$  governs the power-law slope, and  $\beta$

**Table 1.** Summary of the emulator targets used in the halo streaming model pipeline. For each physical ingredient we list the quantity predicted by the emulator, the reduced form used for training, and the surrogate model adopted. “GP” denotes Gaussian Process emulators and “NN” denotes neural-network emulators.

Target Property	Emulated Quantity	Surrogate	Figure
Matter power spectrum $P_{\text{mm}}(k)$	$\alpha(k) \equiv \frac{P_{\text{mm}}(k)}{P_{\text{mm}}^{\text{lin}}(k)}$	GP	Fig. 3
Halo mass function $\frac{dn(M)}{dM}$	$\frac{n(>M)}{n_{\text{ref}}(>M)}$	GP	Fig. 2
Linear halo bias $b(M)$	$b(M)$	GP	Fig. 4
Scale-dependent bias $\mathcal{B}(r M_1, M_2)$	Equation (44)	NN	Figs. 5, 6
Mean radial pairwise velocity	$\frac{m_{10}(r M_1, M_2)}{m_{10}^{\text{lin}}(r M_1, M_2)}$	NN	Fig. 7
Pairwise velocity moments (dispersion $n = 2$ , skewness $n = 3$ , kurtosis $n = 4$ )	$\frac{c^{(n)}(r M_1, M_2)}{[m_{10}(r M_1, M_2)]^n}$	NN	Fig. 8

modifies the exponential cut-off. To ensure the fit captures the intrinsic shape of the mass function without being biased by resolution effects or shot noise, we restrict the fitting range to mass bins satisfying  $N_{\text{thre}} \leq N_{\text{halo}} \leq 10^3 N_{\text{thre}}$ , where  $N_{\text{halo}}$  is the number of simulation particles in a halo. The final processed mass function is constructed as a piecewise function.

Fig. 2 illustrates the performance of this enhanced halo mass function emulator across. The upper panel presents the cumulative HMFs, where points represent the measurements directly from  $N$ -body simulations and solid lines denote the emulator predictions. The dashed lines indicate the high-mass regime where the emulator relies on Schechter-function extrapolation. Distinct colours correspond to different cosmologies within the test set. The lower panel quantifies the accuracy of this emulator, showing the relative difference (as a percentage) between the emulated and simulated results. As shown in the residuals in the lower panel, the emulator achieves sub-percent accuracy over the majority of the mass range.

## 4.2 Matter and halo real-space 2-point correlation functions

In this subsection, we consider the real-space two-point correlation function of dark matter haloes,  $\xi_{\text{hh}}(r|M_1, M_2)$ , measured for haloes in mass bins  $M_1$  and  $M_2$ . To maximise emulation accuracy across a wide range of scales, we again adopt a two-step strategy that separates the modelling of matter clustering from that of halo bias. First, we compute and emulate the nonlinear matter correlation function,  $\xi_{\text{mm}}(r)$ , obtained via an inverse Fourier transform of the simulated matter power spectrum  $P_{\text{mm}}(k)$ . Second, on nonlinear and quasi-linear scales ( $r \leq 40 h^{-1} \text{Mpc}$ ), we emulate the scale-dependent halo bias  $\mathcal{B}(r)$ , defined as

$$\mathcal{B}(r|M_1, M_2) \equiv \frac{\xi_{\text{hh}}(r|M_1, M_2)}{b(M_1)b(M_2)\xi_{\text{mm}}(r)}, \quad (44)$$

where  $b(M)$  is the linear halo bias. This formulation isolates the mass-dependent, nonlinear halo physics into a smoother quantity, reducing the dynamic range and noise level of the emulation target, following the idea of emulating the HMF ratio presented above.

### 4.2.1 Matter power spectrum

An accurate description of the nonlinear matter power spectrum  $P_{\text{mm}}(k)$ , and its Fourier counterpart,  $\xi_{\text{mm}}(r)$ , are needed to model halo clustering on large scales, where the matter field provides the

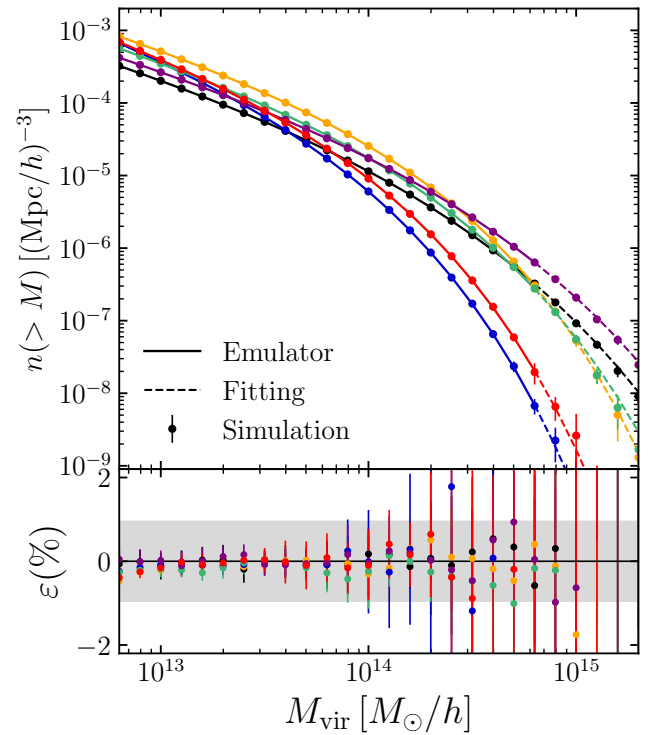


**Figure 2.** Validation of the cumulative halo mass function (cHMF) emulator against the test data set. *Top panel:* The cumulative halo mass functions for different cosmological models (colour-coded). Points show the ground truth from simulations, solid lines represent the emulator predictions, and dashed lines show the Schechter-fitting extrapolation at the high-mass end. *Bottom panel:* The relative percentage residual between the emulator prediction and the simulation data.

baseline signal entering the halo bias and streaming components of the model. Rather than directly emulating the full nonlinear matter power spectra measured from simulations, we construct emulators for the nonlinear boost factor

$$\alpha(k) \equiv \frac{P_{\text{mm}}(k)}{P_{\text{mm}}^{\text{lin}}(k)}, \quad (45)$$

where  $P_{\text{mm}}^{\text{lin}}(k)$  denotes the linear matter power spectrum, which is computed using the Boltzmann solver **CAMB** (Lewis et al. 2000) for each cosmological model in the training and prediction stages.

This choice provides several advantages. First, the linear power spectrum already captures, to some degree, the cosmology dependence through well-understood linear perturbation theory, reducing the dynamic range of the training data. Second, the ratio  $\alpha(k)$  approaches unity on large scales ( $k \rightarrow 0$ ), which stabilises the learning problem and significantly improves accuracy in the low- $k$  regime where small absolute errors in  $P_{\text{mm}}(k)$  would otherwise translate into large relative deviations. The emulator predicts  $\alpha(k)$ , which is then combined with the corresponding linear spectrum to reconstruct the nonlinear matter power spectrum.

Fig. 3 presents validation results on an independent test set not used during training. The upper panel compares emulator predictions (solid curves) with measurements from simulations (points), demonstrating excellent agreement across the entire  $k$  range considered. The lower panel shows the relative residuals, indicating that the emulator achieves  $\sim 1$  per cent accuracy over the scales  $0.01 \leq [k/(h \text{ Mpc}^{-1})] \leq 5.0$ . This level of precision is sufficient for propagating matter clustering uncertainties into the halo-model predictions without introducing a dominant systematic error.

While baryon acoustic oscillation (BAO) features are clearly present in the matter power spectra, our primary objective here is accurate modelling of nonlinear galaxy clustering rather than precision reconstruction of the BAO signal itself. Consequently, we do not introduce additional preprocessing steps specifically designed to optimise the emulation of oscillatory features. Instead, we emulate the full nonlinear boost factor  $\alpha(k)$  directly. This choice simplifies the modelling pipeline and is sufficient for our purposes, as the halo-model predictions developed here primarily rely on broadband clustering information over mildly and strongly nonlinear scales, where residual inaccuracies in the oscillatory component have negligible impact on the final galaxy clustering statistics.

#### 4.2.2 Large-scale linear bias $b(M)$

On sufficiently large scales ( $r \geq 40 h^{-1} \text{ Mpc}$ ), halo clustering is expected to trace the underlying matter distribution in a linear, scale-independent manner. In this regime, the halo-halo correlation function can be approximated as

$$\xi_{\text{hh}}(r|M_1, M_2) \approx b_1(M_1)b_2(M_2)\xi_{\text{mm}}(r), \quad (46)$$

where  $b(M)$  denotes the linear halo bias. We estimate  $b(M)$  directly from the simulations by fitting the ratio of measured correlation functions,

$$b(M) = \left\langle \left[ \frac{\xi_{\text{hh}}(r|M, M)}{\xi_{\text{mm}}(r)} \right]^{1/2} \right\rangle_r, \quad (47)$$

where the average is taken over the separation range  $40 \leq r/(h^{-1} \text{ Mpc}) \leq 80$ . The average weights are chosen to be inversely proportional to the propagated variance of the ratio across the five simulation realisations of each cosmological model. This ensures that scales with higher signal-to-noise ratios dominate the fit. This range is selected to exclude nonlinear halo exclusion effects at smaller separations while limiting the impact of sample variance at very large scales in finite-volume simulations.

#### 4.2.3 Mass extrapolation

A major challenge in emulating the mass dependence of halo clustering statistics arises from the scarcity of high-mass haloes. In

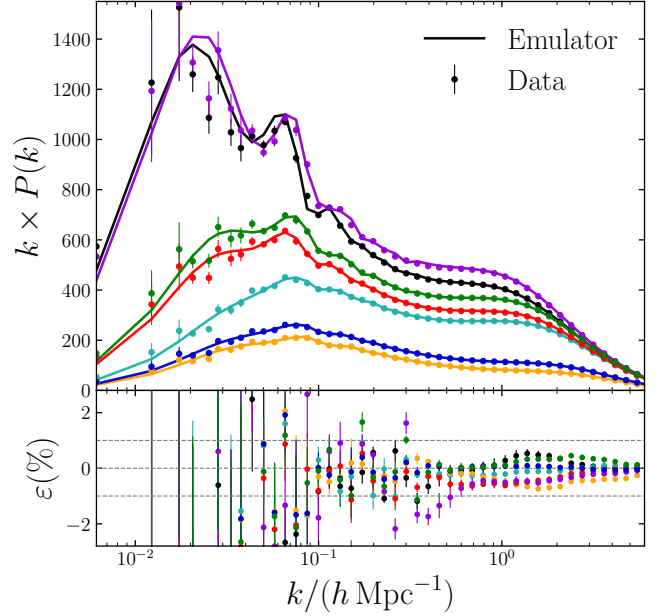


**Figure 3.** Validation of the matter power spectrum emulator. *Top panel:* comparison between emulator predictions (solid lines) and simulation measurements (points) for the cosmologies in the test data set. Colours encode different cosmological models. *Bottom panel:* relative difference between emulator and simulation results. The emulator reproduces the nonlinear matter power spectrum with an accuracy of approximately 1% across the scale range used in the analysis. 

the DEGRACE-pilot simulations, shot noise becomes dominant for halo mass  $M \gtrsim 10^{14} h^{-1} M_{\odot}$ , rendering direct emulation of  $\xi_{\text{hh}}(r|M_1, M_2)$  reliable only in a narrow mass range. To enable robust predictions for these rare objects, we implement a physically motivated extrapolation scheme based on the linear halo bias.

To extend the bias model into the cluster-mass regime ( $M = 10^{14} - 10^{15} h^{-1} M_{\odot}$ ), where direct measurements are already noise dominated, we adopt the functional form proposed by Tinker et al. (2010), which expresses the bias as a function of the peak height  $\nu$ ,

$$b(\nu) = 1 - A \frac{\nu^a}{\nu^a + \delta_c^a} + B\nu^b + C\nu^c, \quad (48)$$

where  $\delta_c = 1.686$  is the critical overdensity for spherical collapse. The peak height is defined as  $\nu \equiv \delta_c/\sigma(M)$ , with  $\sigma(M)$  denoting the root-mean-square fluctuation of the linear density field smoothed on the Lagrangian scale  $R(M) = [3M/(4\pi\bar{\rho}_m)]^{1/3}$ .

We calibrate this model by fitting Equation (48) to the simulated bias measurements in the well-sampled mass range  $10^{12.4} < M/(h^{-1} M_{\odot}) < 10^{13.8}$ . To avoid unphysical behaviour in the high-mass extrapolation, we adopt a constrained fitting strategy in which the shape parameters controlling the asymptotic scaling at large  $\nu$  are fixed close to the reference values of Tinker et al. (2010) ( $a = 0.132$ ,  $b = 1.5$ ,  $c = 2.4$ ), while allowing only the normalisation coefficients ( $A$ ,  $B$ ,  $C$ ) to vary. This ensures that the extrapolated bias retains the expected  $\nu^2$  scaling for rare density peaks (Sheth & Tormen 1999), while still remaining flexible enough to accommodate the halo definition and cosmology variations in the simulation suite adopted here. The resulting calibrated model is then used to predict  $b(M)$  for all haloes with  $M \geq 10^{13.8} h^{-1} M_{\odot}$ .

Fig. 4 illustrates the behaviour of the linear halo bias as a function of halo mass at  $z = 0.25$  for the fiducial *Planck* cosmology

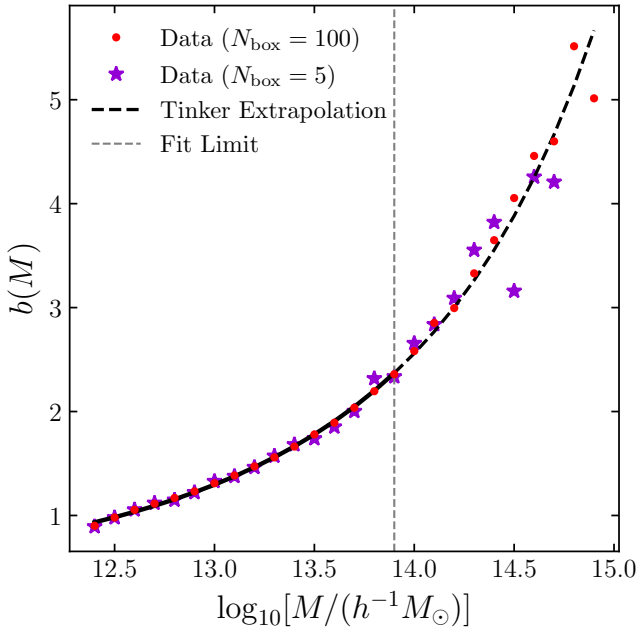


**Figure 4.** Linear halo bias as a function of halo mass at  $z = 0.25$  for the fiducial *Planck* cosmology (Planck Collaboration et al. 2016). The purple stars represent measurements from a subset of five realisations ( $N_{\text{box}} = 5$ ), mimicking the noise level of the training data set. The red points show the ground truth derived from the full suite of 100 realisations. The black curve follows the Tinker et al. (2010) bias model: the solid section marks the range used to fit the normalisation parameters, while the dashed section to the right of the vertical line represents the extrapolation to higher masses. The vertical grey dashed line indicates the upper mass limit of the fitting region. The extrapolation demonstrates excellent agreement with the high-mass validation data.

(Planck Collaboration et al. 2016). Measurements obtained from a reduced set of five simulation realisations are shown in purple stars as representative of the noise level in the emulator training data. In contrast, the bias measured from the full ensemble of 100 realisations (red points) provides a high-precision reference against which the modelling can be assessed. The black curve shows the bias predicted by the Tinker et al. (2010) fitting formula, with the solid segment indicating the mass range used to calibrate the parameters. The vertical grey dashed line marks the upper boundary of this fitting region, beyond which the model is extrapolated (black dashed curve). The extrapolated bias remains in excellent agreement with the high-mass validation measurements, demonstrating that the parametric model, when anchored on the well-measured low-mass regime, provides a reliable mass extension of halo bias and 2PCF in the sparse cluster-mass tail.

#### 4.2.4 The scale-dependent bias and the full halo two-point correlation function

Fig. 5 presents a representative validation of the halo 2-point correlation function emulator using a cosmological model drawn from the independent test data set. The comparison demonstrates that the emulator accurately reproduces the real-space halo clustering measured in the  $N$ -body simulations across a wide range of separations.

On small and intermediate scales, the prediction is governed by the emulator for the scale-dependent bias  $\mathcal{B}(r|M_1, M_2)$  defined in Equation (44), which captures nonlinear halo exclusion and scale-

dependent clustering effects. Toward large separations, the model transitions smoothly to the linear-bias approximation. This stitching procedure enforces physical consistency in the linear regime while preserving the flexibility of the nonlinear emulator on smaller scales. The resulting prediction achieves sub-percent agreement with simulation measurements over the range where the signal is well resolved. The larger relative fluctuations observed at the largest separations arise because the correlation function approaches zero, amplifying statistical noise in the ratio.

Fig. 6 illustrates the behaviour of the emulator for the scale-dependent halo bias  $\mathcal{B}(r|M_1, M_2)$ . To visualise its parameter dependence, the left panel shows results in a fixed cosmology from the test set and fixed mass  $M_1 = 10^{13.5} h^{-1} M_\odot$  while varying  $M_2$ . The right panel fixes both halo masses at  $M_1 = M_2 = 10^{13.5} h^{-1} M_\odot$  and varies the cosmological model across the test sample. These panels demonstrate that the emulator captures both the mass and the cosmology dependence of the scale-dependent bias in a smooth and physically consistent manner.

The halo 2PCF measured in differential mass bins can be noisy at high masses where halo abundances are low. Consequently, the pointwise accuracy of the  $\mathcal{B}(r|M_1, M_2)$  emulator is slightly worse than other emulated quantities in the pipeline. However, the halo model ultimately requires correlation functions integrated over finite mass ranges. As shown in Fig. 5, these integrated halo 2PCFs are substantially smoother, and the final emulator predictions retain percent-level accuracy. This behaviour can be understood from the differential results in Fig. 6, where residuals fluctuate around zero; when integrated over halo mass within halo-model expressions (e.g. galaxy clustering predictions), positive and negative deviations partially cancel, leading to a stable and accurate final prediction.

### 4.3 Halo pairwise velocity moments

We construct emulators for halo pairwise velocity moments up to fourth order,

$$\{m_{10}, c_{20}, c_{02}, c_{30}, c_{12}, c_{40}, c_{22}, c_{04}\}(r|M_1, M_2), \quad (49)$$

which fully specify the non-Gaussian pairwise velocity statistics entering the halo streaming model. The measurements are obtained from  $N$ -body simulations on differential halo mass grids and averaged over five realisations to reduce sample variance. As velocity moments exhibit large dynamic range and strong cosmology dependence, we adopt a physics-informed rescaling before emulation.

On large scales, the mean radial pairwise velocity follows from linear perturbation theory and pair conservation. Assuming unbiased halo velocities, the linear-theory prediction for two halo populations with masses  $(M_1, M_2)$  is

$$m_{10}^{\text{hh,lin}}(r|M_1, M_2) = -\frac{2}{3} a H f r \left( \frac{b(M_1) + b(M_2)}{2} \right) \bar{\xi}_{\text{mm}}(r), \quad (50)$$

where  $f = d \ln D / d \ln a$  is the linear growth rate and  $\bar{\xi}_{\text{mm}}(r)$  is the matter correlation function averaged over a sphere of radius  $r$ . In practice,  $\bar{\xi}_{\text{mm}}$  is computed from the linear matter correlation function predicted by the matter  $\alpha$  emulator. This construction provides a physically motivated large-scale anchor for the velocity field. Rather than emulating  $m_{10}$  directly, we define a reduced quantity

$$\omega(r|M_1, M_2) \equiv \frac{m_{10}(r|M_1, M_2)}{m_{10}^{\text{lin}}(r|M_1, M_2)}, \quad (51)$$

which approaches unity on large scales and varies smoothly with cosmology and halo mass. This physics-informed normalisation

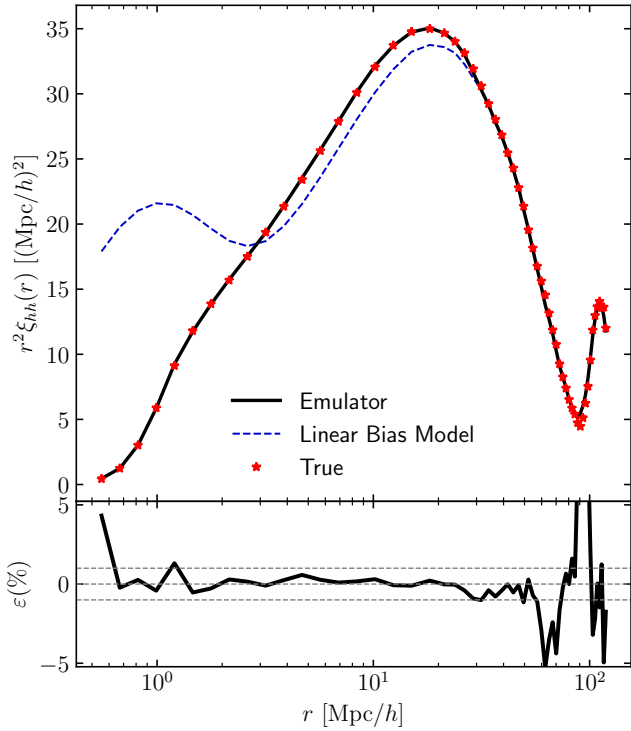


**Figure 5.** Comparison between the simulated and emulated halo two-point correlation function for a representative cosmological model in the test data set. The upper panel shows the real-space correlation function  $\xi_{\text{hh}}(r)$  scaled by  $r^2$  for haloes with  $M \geq 10^{12.5} h^{-1} M_{\odot}$ . Red stars denote measurements from the  $N$ -body simulations, while the solid black curve shows the emulator prediction. The thin blue dashed curve corresponds to the large-scale linear bias approximation. The final prediction smoothly stitches the small-scale emulator output to the linear-theory limit to improve signal-to-noise on large scales. The lower panel shows the relative difference between emulator and simulations. Sub-percent agreement is achieved over the range where  $\xi_{\text{hh}}(r)$  is well measured; apparent large deviations at the largest separations arise because  $\xi_{\text{hh}}(r)$  approaches zero.

substantially improves emulator stability and extrapolation behaviour.

Higher-order moments span several orders of magnitude and may change sign across scales. To stabilise the learning problem, all velocity moments are expressed in terms of reduced variables scaled by powers of the first-order moment  $m_{10}$ ,

$$\left(\frac{c_{20}}{m_{10}^2}\right)^{1/2}, \left(\frac{c_{30}}{m_{10}^3}\right)^{1/3}, \left(\frac{c_{40}}{m_{10}^4}\right)^{1/4}, \quad (52)$$

with analogous scalings applied to other higher-order moments.

The emulation is performed using a neural-network model following the same modular design as the halo bias emulator. Input and target variables are normalised using statistics derived from the training set only, preventing information leakage between splits. After prediction, the inverse transformation is applied to recover the physical velocity moments required by the streaming model.

Fig. 7 shows emulator predictions for the mean pairwise velocity. The emulator captures smooth variations with halo mass and cosmology despite the intrinsic noise present in differential mass-bin measurements. As in the halo clustering emulator, residual errors fluctuate around zero and partially cancel once integ-

rated within halo-model expressions, yielding stable predictions for galaxy clustering observables.

Fig. 8 presents predictions for higher-order halo pairwise velocity moments, including the dispersion ( $c_{02}$ ), skewness ( $c_{30}$ ), and kurtosis ( $c_{04}$ ). These quantities probe progressively non-Gaussian aspects of the pairwise velocity distribution and are therefore intrinsically noisier than the mean velocity. Nevertheless, after applying the physics-informed rescaling described above, the emulator recovers smooth and physically consistent trends with separation and cosmology. The residual fluctuations primarily reflect measurement noise in differential mass bins and do not propagate significantly into halo-model predictions, where the moments enter through integrals over halo mass. This demonstrates that the adopted reduced parametrisation provides a stable basis for emulating the full hierarchy of velocity moments required by the streaming model.

## 5 MODEL VALIDATION

Fig. 9 shows the halo streaming predictions for the galaxy redshift-space distortion monopole and quadrupole, together with measurements from the simulations. The model accurately reproduces both multipoles across a broad range of scales, demonstrating that the emulator-based description of halo clustering and velocity statistics provides a consistent mapping from real to redshift space. The decomposition into galaxy pair types clarifies the physical origin of the signal: on large scales the monopole and quadrupole are dominated by the two-halo central-central contribution, reflecting coherent large-scale flows, while on smaller separations the one-halo central-satellite and satellite-satellite terms become more important and drive the suppression of the quadrupole through virial motions. The agreement between data and model predictions across the transition between one- and two-halo regimes indicates that the halo streaming framework captures both linear Kaiser effects and nonlinear Fingers-of-God behaviour within a unified model.

To further validate the accuracy and internal consistency of this emulator-based halo streaming model, we perform an end-to-end parameter recovery test using Markov chain Monte Carlo inference. The goal of this test is to assess whether the full modelling pipeline, including the emulators for halo properties, can recover the true cosmological and halo occupation distribution parameters.

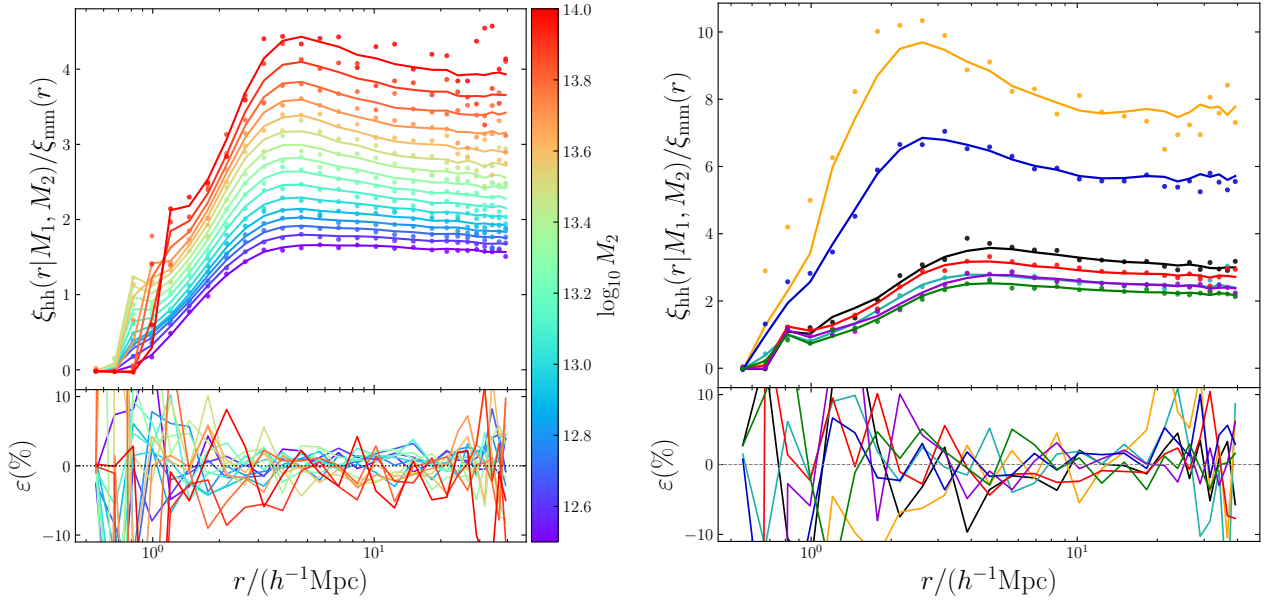
We define the Gaussian likelihood as

$$\ln \mathcal{L}(\mathcal{C}, \mathcal{G} | \mathbf{d}_{\text{obs}}) \propto \left[ \mathbf{d}_{\text{obs}} - \mathbf{d}_{\text{model}}(\mathcal{C}, \mathcal{G}) \right]^T \mathbf{C}^{-1} \left[ \mathbf{d}_{\text{obs}} - \mathbf{d}_{\text{model}}(\mathcal{C}, \mathcal{G}) \right], \quad (53)$$

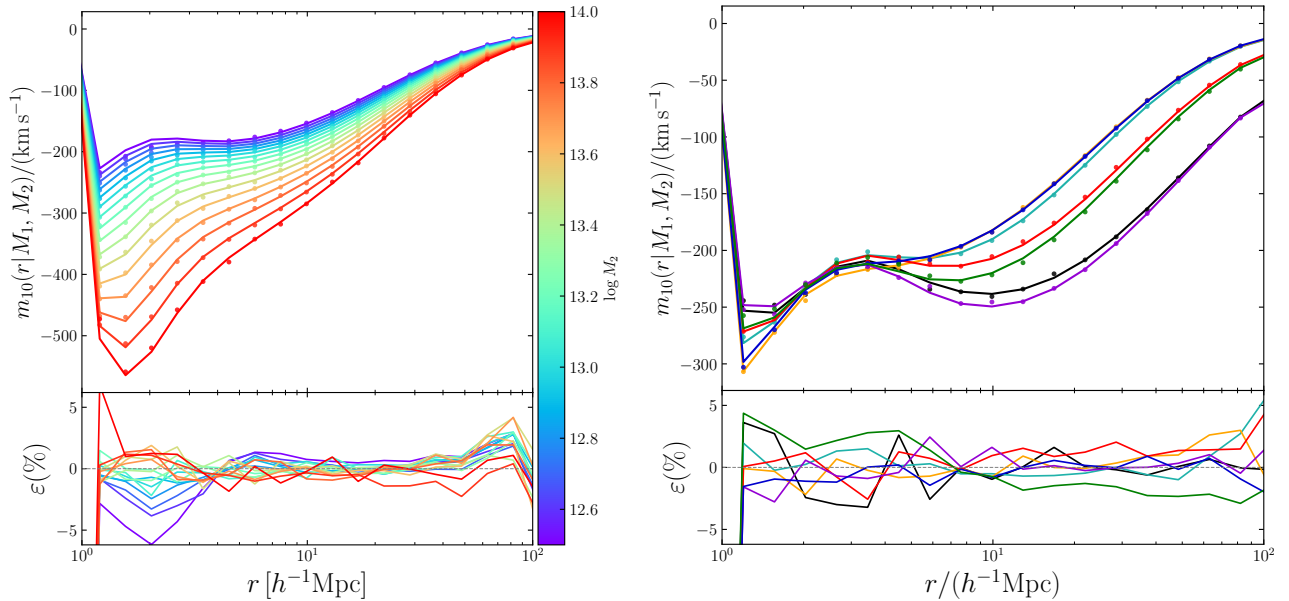
where  $\mathbf{d}_{\text{obs}}$  is the ‘‘observed’’ data vector measured from the 100 realisations of simulations with the fiducial *Planck* cosmology, and  $\mathbf{d}_{\text{model}}(\mathcal{C}, \mathcal{G})$  denotes the prediction of the halo streaming model for a given set of cosmological parameters  $\mathcal{C}$  and HOD parameters  $\mathcal{G}$ . The covariance matrix  $\mathbf{C}$  is estimated from the AbacusSummit (Maksimova et al. 2021) small box simulations and is kept fixed.

Fig. 10 shows the posterior distributions from this likelihood. The contours indicate the joint and marginal constraints on all cosmological and HOD parameters, while the reference lines mark the true input values used to generate the mock data. All parameters are successfully recovered within the one sigma credible intervals, with no evidence for systematic shifts or biased degeneracy directions. This shows that the emulated halo streaming model provides an unbiased mapping between parameter space and observable space.

Overall, this recovery test confirms that the modular emulation framework preserves the cosmological and astrophysical information content of the clustering signal, while maintaining sufficient



**Figure 6.** Emulator predictions for the scale-dependent halo bias  $\xi_{\text{hh}}(r|M_1, M_2)/\xi_{\text{mm}}(r)$ . *Left panel:* fixed cosmology and  $M_1 = 10^{13.5} h^{-1} M_\odot$  with varying  $M_2$ , as indicated by the colour bar. *Right panel:* fixed halo masses ( $M_1 = M_2 = 10^{13.5} h^{-1} M_\odot$ ) with varying cosmologies from the test set (note in this case the line colour denotes different cosmological parameter sets). The lower panel shows the residuals between the emulator and the direct measurement. The emulator captures smooth variations with both halo mass and cosmology despite the intrinsic noise present in differential mass-bin measurements. 



**Figure 7.** Emulator predictions for the mean halo pairwise velocity moment  $m_{10}(r|M_1, M_2)$ . *Left panel:* fixed cosmology with  $M_1 = 10^{13.1} h^{-1} M_\odot$  and varying  $M_2$  as indicated by the colour bar. *Right panel:* fixed halo masses ( $M_1 = M_2 = 10^{13.1} h^{-1} M_\odot$ ) with varying cosmologies from the test set. The emulator reproduces smooth mass and cosmology dependence despite noise in differential measurements. 

accuracy for joint inference. The successful parameter recovery provides a critical validation of the model and supports its application to precision analyses of spectroscopic galaxy surveys.

## 6 DISCUSSION AND CONCLUSIONS

We have developed an emulator-based halo streaming model that provides an accurate, interpretable, and computationally efficient

description of nonlinear redshift-space distortions in galaxy clustering. By combining the halo model with the streaming-model formalism and predicting each building block ingredient using emulators trained on  $N$ -body simulations, we construct a unified framework capable of predicting the full-shape anisotropic clustering signal across a wide range of scales and tracer populations.

A key aspect of our work is the principle of *modular emulation*. Rather than directly emulating the redshift space observables, which would require generating a large number of mock galaxy

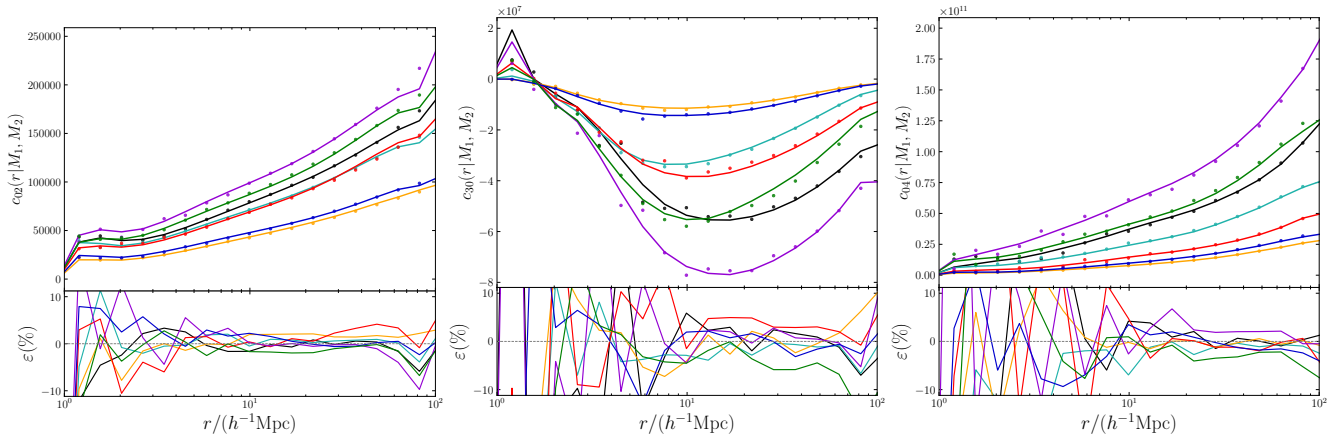


**Figure 8.** Emulator predictions for representative higher-order halo pairwise velocity moments: dispersion ( $c_{02}$ , left), skewness ( $c_{30}$ , centre), and kurtosis ( $c_{04}$ , right). Halo masses are fixed at  $M_1 = M_2 = 10^{13.1} h^{-1} M_\odot$  while colours denote different cosmological models from the test set. Despite the increased noise present in differential mass-bin measurements, the emulator captures smooth scale and cosmology dependence across all moments. 

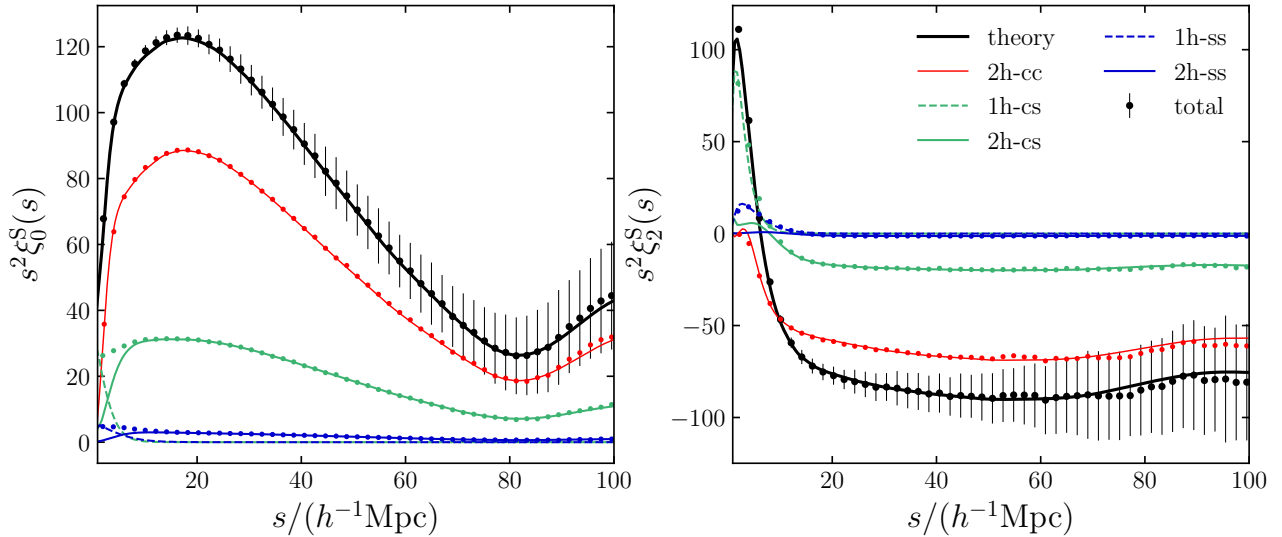


**Figure 9.** Predictions of the emulator-based halo streaming model for the galaxy redshift-space correlation function multipoles at  $z = 0.25$ . The left panel shows the monopole  $\xi_0^S(s)$ , while the right panel shows the quadrupole  $\xi_2^S(s)$ . Points denote measurements from simulations and curves show model predictions. Black lines correspond to the total galaxy-galaxy clustering signal. Contributions from different galaxy pair types are shown separately: central-central (red), central-satellite (green), and satellite-satellite (blue). Solid lines indicate two-halo terms and dashed lines indicate one-halo terms. 

catalogues,  $N_{\text{cosmology}} \times N_{\text{HOD}}$ , we focus instead on the physical building blocks of the model, namely the halo mass function, real space halo correlation functions, and pairwise velocity moments. This strategy preserves physical transparency and interpretability while allowing each component to be optimized, validated, and extended independently. In practice, such modularity yields greater robustness and flexibility than end to end emulation approaches, particularly when varying tracer properties or incorporating additional physical effects. nevertheless, we must adopt direct emulation in cases where analytical decompositions are impractical, such as for void (e.g. Radinovic et al. 2023; Fraser et al. 2025) and density split statistics (e.g. Cuesta-Lazaro et al. 2024; Paillas et al. 2024).

The halo streaming model systematically decomposes the RSD signal into contributions from different galaxy types and halo environments. This provides clear physical insight into the origin of nonlinear RSD effects. Small-scale Fingers-of-God features are

primarily sourced by satellite motions within haloes, while large-scale anisotropies are governed by coherent halo bulk flows induced by gravity. By explicitly modelling these components and their associated velocity moments, the framework captures the transition from linear to deeply nonlinear scales in a controlled and physically motivated manner. The agreement with simulation-based mock catalogues demonstrates that this approach can recover the full-shape RSD signal without discarding valuable small-scale information.

An important advantage of the present framework is its computational efficiency. Once trained, the emulators enable rapid predictions of all halo-model ingredients, allowing the full redshift-space correlation function to be evaluated without generating full HOD catalogues. This efficiency makes the model well suited for exploring baseline extensions and performing cosmological parameter inference. At the same time, the separation between cosmological

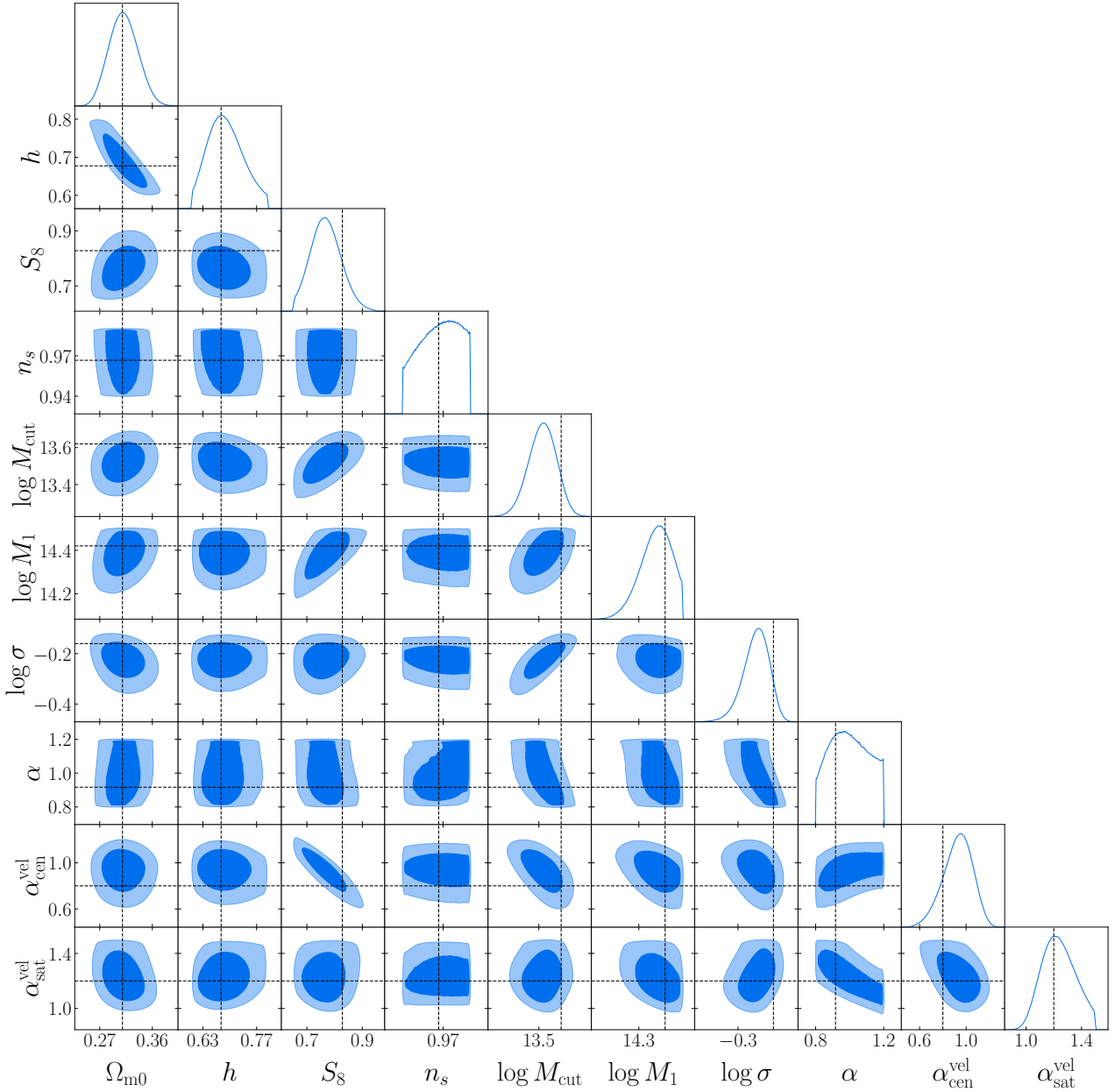


**Figure 10.** Corner plot from the MCMC recovery test using the halo streaming model. The contours show the joint and marginal posterior distributions of all cosmological and halo occupation distribution parameters, with the input values indicated by vertical and horizontal reference lines. All parameters are successfully recovered within the  $1\sigma$  credible intervals, demonstrating that the emulator based model is unbiased and retains the cosmological information required for joint inference of cosmology and galaxy bias.

dependence and tracer modelling also facilitates joint analyses of cosmology and galaxy-halo connection parameters.

Although the model achieves high accuracy within the regime explored in this work, several limitations and avenues for improvement remain. First, the accuracy of the predictions is ultimately bounded by the fidelity and coverage of the training simulations. Extensions to larger cosmological parameter spaces, different redshifts, or alternative gravity models will require additional simulation suites. We plan to run suites of simulations for alternative gravity theories such as  $f(R)$  gravity and Dvali-Gabadadze-Porrati (DGP) model. Second, the current implementation assumes standard halo definitions and parametric HOD prescriptions; more flexible or assembly-biased galaxy-halo connections could be incor-

porated in future work. Third, baryonic effects are not explicitly incorporated and may impact clustering and velocity statistics on scales  $r \lesssim 1-2 h^{-1} \text{Mpc}$ , where processes such as gas cooling, star formation, and feedback from supernovae and active galactic nuclei can modify the internal structure of haloes and the distribution and velocities of galaxies relative to the dark matter (e.g. Mead et al. 2015; Chisari et al. 2019).

The halo streaming framework presented here is readily extensible. The formalism can be applied to any galaxy tracer, three-point correlation function, or alternative tracers such as neutral hydrogen and quasars. Incorporating modified gravity models and environmental dependencies of galaxy occupation are natural next steps. Moreover, the modular structure makes it straightforward to replace

or augment individual ingredients as improved simulations or theoretical models become available.

In summary, we have demonstrated that combining simulation-based calibration with a physically motivated halo streaming model provides a powerful route toward precision modelling of nonlinear redshift-space distortions. This approach bridges the gap between analytic theory and numerical simulations, retaining interpretability while achieving the accuracy required by forthcoming surveys. With its flexibility, efficiency, and transparent physical foundation, the framework developed in this work offers a robust tool for extracting cosmological information from the full statistical power of next-generation large-scale structure data sets such as DESI and *Euclid*.

## ACKNOWLEDGEMENTS

C-ZR and BL are funded by the ERC Advanced Grant UNCA (UKRI Frontiers Research Guarantee No. EP/Z533877/1). BL, CMB and SB acknowledge support from the UK STFC Consolidated Grant ST/X001075/1. C-ZR and DFM thank the Research Council of Norway for their support and the resources provided by UNINETT Sigma2 – the National Infrastructure for High-Performance Computing and Data Storage in Norway. S.B. is supported by the UKRI Future Leaders Fellowship [grant numbers MR/V023381/1 and UKRI2044]. This work used the DiRAC@Durham facility managed by the Institute for Computational Cosmology on behalf of the STFC DiRAC HPC Facility ([www.dirac.ac.uk](http://www.dirac.ac.uk)). The equipment was funded by BEIS capital funding via STFC capital grants ST/K00042X/1, ST/P002293/1, ST/R002371/1 and ST/S002502/1, Durham University and STFC operations grant ST/R000832/1. DiRAC is part of the National e-Infrastructure.

## DATA AVAILABILITY

The data underlying this article will be shared on reasonable request to the corresponding author. The processed data and plotting scripts are available in the *freyja* package. We also provide direct access to the source code for each figure via the clickable icon appended to the figure captions.

## References

- Alom M. Z., et al., 2019, *Electronics*, 8
- Amendola L., et al., 2013, *Living Reviews in Relativity*, 16, 6
- Asgari M., Mead A. J., Heymans C., 2023, *The Open Journal of Astrophysics*, 6, 39
- Azzalini A., Capitanio A., 2009, *arXiv e-prints*, p. [arXiv:0911.2342](https://arxiv.org/abs/0911.2342)
- Benson A. J., Cole S., Frenk C. S., Baugh C. M., Lacey C. G., 2000, *MNRAS*, 311, 793
- Berlind A. A., et al., 2003, *ApJ*, 593, 1
- Bishop C. M., et al., 1995, *Neural networks for pattern recognition*. Oxford university press
- Chisari N. E., et al., 2019, *The Open Journal of Astrophysics*, 2, 4
- Cole S., et al., 2005, *MNRAS*, 362, 505
- Conroy C., Wechsler R. H., Kravtsov A. V., 2006, *ApJ*, 647, 201
- Cooray A., Sheth R., 2002, *Phys. Rep.*, 372, 1
- Cuesta-Lazaro C., Li B., Eggemeier A., Zarrouk P., Baugh C. M., Nishimichi T., Takada M., 2020, *MNRAS*, 498, 1175
- Cuesta-Lazaro C., et al., 2023, *MNRAS*, 523, 3219
- Cuesta-Lazaro C., et al., 2024, *MNRAS*, 531, 3336
- DESI Collaboration et al., 2016, *arXiv e-prints*, p. [arXiv:1611.00036](https://arxiv.org/abs/1611.00036)
- Davis M., Peebles P. J. E., 1983, *ApJ*, 267, 465
- DeRose J., et al., 2019, *ApJ*, 875, 69
- DeepMind et al., 2020, The DeepMind JAX Ecosystem, <http://github.com/google-deeppmind>
- Dvornik A., et al., 2023, *A&A*, 675, A189
- Euclid Collaboration et al., 2025, *A&A*, 697, A1
- Fisher K. B., 1995, *ApJ*, 448, 494
- Foreman-Mackey D., et al., 2024, *dfm/tinygp: The tiniest of Gaussian Process libraries*, doi:10.5281/zenodo.10463641, <https://doi.org/10.5281/zenodo.10463641>
- Fraser T. S., Paillas E., Percival W. J., Nadathur S., Radinović S., Winther H. A., 2025, *J. Cosmology Astropart. Phys.*, 2025, 001
- Guzzo L., et al., 2008, *Nature*, 451, 541
- Hawkins E., et al., 2003, *MNRAS*, 346, 78
- Hearin A. P., Zentner A. R., van den Bosch F. C., Campbell D., Tollerud E., 2016, *MNRAS*, 460, 2552
- Heitmann K., White M., Wagner C., Habib S., Higdon D., 2010, *ApJ*, 715, 104
- Hernández-Aguayo C., Prada F., Baugh C. M., Klypin A., 2021, *MNRAS*, 503, 2318
- Kaiser N., 1987, *MNRAS*, 227, 1
- Klypin A., Prada F., 2018, *MNRAS*, 478, 4602
- Klypin A., et al., 2021, *Mon. Not. Roy. Astron. Soc.*, 504, 769
- Kravtsov A. V., Berlind A. A., Wechsler R. H., Klypin A. A., Gottlöber S., Allgood B., Primack J. R., 2004, *ApJ*, 609, 35
- Kuruvilla J., Porciani C., 2018, *MNRAS*, 479, 2256
- Kuruvilla J., Porciani C., 2020, *J. Cosmology Astropart. Phys.*, 2020, 043
- Laureijs R., et al., 2011, *arXiv e-prints*, p. [arXiv:1110.3193](https://arxiv.org/abs/1110.3193)
- Lewis A., Challinor A., Lasenby A., 2000, *ApJ*, 538, 473
- Mahony C., et al., 2022, *MNRAS*, 515, 2612
- Maksimova N. A., Garrison L. H., Eisenstein D. J., Hadzhiyska B., Bose S., Satterthwaite T. P., 2021, *MNRAS*, 508, 4017
- Matoušek J., 1998, *Journal of Complexity*, 14, 527
- Mead A. J., Verde L., 2021, *MNRAS*, 503, 3095
- Mead A. J., Peacock J. A., Heymans C., Joudaki S., Heavens A. F., 2015, *MNRAS*, 454, 1958
- Miyatake H., et al., 2020, *arXiv e-prints*, p. [arXiv:2101.00113](https://arxiv.org/abs/2101.00113)
- Murray S. G., Power C., Robotham A. S. G., 2013, *Astronomy and Computing*, 3, 23
- Murray S. G., Diemer B., Chen Z., Neuhold A. G., Schnapp M. A., Peruzzi T., Blevins D., Engelman T., 2021, *Astronomy and Computing*, 36, 100487
- Nishimichi T., et al., 2019, *ApJ*, 884, 29
- Paillas E., et al., 2024, *Mon. Not. Roy. Astron. Soc.*, 531, 898
- Peacock J. A., et al., 2001, *Nature*, 410, 169
- Peebles P. J. E., 1980, *The large-scale structure of the universe*
- Planck Collaboration et al., 2016, *A&A*, 594, A13
- Radinovic S., et al., 2023, *Astron. Astrophys.*, 677, A78
- Ruan C.-Z., Cuesta-Lazaro C., Eggemeier A., Hernández-Aguayo C., Baugh C. M., Li B., Prada F., 2022a, *MNRAS*, 514, 440
- Ruan C.-Z., Hernández-Aguayo C., Li B., Arnold C., Baugh C. M., Klypin A., Prada F., 2022b, *J. Cosmology Astropart. Phys.*, 2022, 018
- Schmidt F., 2016, *Phys. Rev. D*, 93, 063512
- Scoccimarro R., 2004, *Phys. Rev. D*, 70, 083007
- Seljak U., 2000, *MNRAS*, 318, 203
- Sheth R. K., Tormen G., 1999, *MNRAS*, 308, 119
- Sheth R. K., Mo H. J., Tormen G., 2001, *MNRAS*, 323, 1
- Sobol I. M., 1967, *USSR Computational Mathematics and Mathematical Physics*, 7, 86
- Tinker J. L., 2007, *MNRAS*, 374, 477
- Tinker J. L., Weinberg D. H., Zheng Z., Zehavi I., 2005, *ApJ*, 631, 41
- Tinker J. L., Robertson B. E., Kravtsov A. V., Klypin A., Warren M. S., Yepes G., Gottlöber S., 2010, *ApJ*, 724, 878
- Williams C. K., Rasmussen C. E., 2006, *Gaussian processes for machine learning*. MIT press Cambridge, MA
- Zhai Z., et al., 2019, *ApJ*, 874, 95
- Zhang A., Lipton Z. C., Li M., Smola A. J., 2021, *arXiv e-prints*, p. [arXiv:2106.11342](https://arxiv.org/abs/2106.11342)
- Zheng Z., 2004, *ApJ*, 610, 61

- Zheng Z., Guo H., 2016, *MNRAS*, 458, 4015  
Zheng Z., et al., 2005, *ApJ*, 633, 791  
Zheng Z., Coil A. L., Zehavi I., 2007, *ApJ*, 667, 760  
Zu Y., Weinberg D. H., 2013, *MNRAS*, 431, 3319  
van den Bosch F. C., More S., Cacciato M., Mo H., Yang X., 2013, *MNRAS*, 430, 725

This paper has been typeset from a  $\text{\TeX/L\AA\TeX}$  file prepared by the author.